crystals

MDPI

Article

Chiral π-Conjugated Liquid Crystals: Impacts of Ethynyl Linker and Bilateral Symmetry on the Molecular Packing and Functions

Atsushi Seki *, Kazuki Shimizu and Ken'ichi Aoki

Department of Chemistry, Faculty of Science Division II, Tokyo University of Science, 1-3 Kagurazaka, Shinjuku-ku, Tokyo 162-8601, Japan

* Correspondence: a_seki_3@rs.tus.ac.jp; Tel.: +81-3-3260-4271

Abstract: Recently, various chiral aromatic compounds, including chiral π-conjugated liquid crystals, have been developed for their unique photofunctions. One of the typical photofunctions is the bulk photovoltaic effect of ferroelectric π-conjugated liquid crystals, which integrates a polar environment based on molecular chirality with an extended π-conjugation system. Tuning the spectral properties and molecular packing is essential for improving the optical functions of the chiral π-conjugated liquid crystals. Herein, we examined the effects of an ethynyl linker and bilateral symmetry on the liquid-crystalline (LC) properties and π-conjugated system through detailed characterization via polarizing optical microscopy, differential scanning calorimetry, and X-ray diffraction analysis. The spreading of the π-conjugated system was evaluated using UV–vis absorption and photoluminescence spectroscopy. Bilateral symmetry affects the LC and photoluminescent properties. Hetero-substitution with a sparse ethynyl linker likely allows the formation of an interdigitated smectic LC structure. Because the molecular packing and photophysical properties can affect the photo- and electrical functions, we believe this study can promote the molecular design of novel functional π-conjugated materials, such as chiral ferroelectric π-conjugated liquid crystals, exhibiting the bulk photovoltaic effect.

Keywords: molecular chirality; π-conjugated compound; liquid crystal

Citation: Seki, A.; Shimizu, K.; Aoki, K. Chiral π-Conjugated Liquid Crystals: Impacts of Ethynyl Linker and Bilateral Symmetry on the Molecular Packing and Functions. *Crystals* **2022**, *12*, 1278. https://doi.org/10.3390/cryst12091278

Academic Editor: Charles Rosenblatt

Received: 9 August 2022
Accepted: 6 September 2022
Published: 9 September 2022

1. Introduction

Molecular chirality can induce the formation of hierarchical suprastructures, which acts as platforms for biological, pharmacological, chemical, and physical functions [1–7]. A broken-symmetry structure is a self-organized structure that reflects the molecular chirality. Symmetry reduction leads to the stabilization of polar structures. Thus, ferroelectricity can be observed in such chiral suprastructures [8–10]. Another representative chiral supramolecular system is the helical self-assembly. The absolute configuration of the chiral molecules labeled (*R*) or (*S*) reflects their helical structure and axis. Because the helical conformation due to inherent molecular chirality is known to contribute to various functionalities of self-assembled materials, chiral materials, including chiral polymers [6,11], chiral supramolecular polymers [6,12], and chiral liquid crystals (CLCs) [2,13–15], have been extensively developed and studied. In particular, CLCs show sensitive responses to external stimuli, such as temperature and electric fields, because of their dynamic nature [14,15]. In recent years, we have focused on chiral smectic liquid crystals resulting from introducing molecular chirality into smectic liquid crystal systems [16–19]. From both basic scientific and engineering standpoints, the most important and beneficial chiral smectic liquid crystal is a ferroelectric liquid-crystalline material that exhibits a chiral smectic C (SmC*) phase. In the neutral SmC* phase, the CLC molecules form a tilted-layer structure with helical twisting of the molecular axis along the normal layer. When an electric field is applied to planar-aligned CLC molecules with a transverse dipole moment in the SmC* phase, molecular reorientation should occur

to unwind helical structures. Because molecular chirality can stabilize the polar structure owing to the reduction of structural symmetry, ferroelectric properties are often observed in the SmC* phase. Conventional CLCs have been investigated for their applications such as in optical sensors [20] and high-speed liquid-crystal displays [21]. While conventional CLCs are generally insulators, chiral π-conjugated liquid crystals have the potential to be unique photofunctional materials [16–19,22]. Many π-conjugated liquid crystals have been synthesized, and their electronic charge carrier transport properties have been explored as liquid-crystalline (LC) semiconductors [23–28]. LC materials have some advantages such as improved solubility in common organic solvents, the control of molecular orientation, and the formation of uniform thin films against inorganic semiconductors. Therefore, LC semiconductors have been frequently used as active materials in optoelectronic devices such as bulk heterojunction organic photovoltaic devices [29,30], organic light-emitting diodes [31–33], and organic thin-film transistors [34–36].

This study aimed to develop chiral π-conjugated liquid crystals for novel optoelectronic materials. Recently, exciting applications of chiral π-conjugated liquid crystals have been reported. For instance, Funahashi et al. developed electric-field-responsive CLCs that exhibited an SmC* phase. As terthiophene-based CLCs show ferroelectricity and photoconductivity in the SmC* phase, the combined effect of spontaneous polarization and carrier transport results in a bulk photovoltaic effect in the LC phase [37]. The bulk photovoltaic effect based on molecular chirality is a newly discovered type of ferroelectric photovoltaic (FePV) effect, which is classified as one of the bandgap-independent photovoltaic effects [38–41]. As the FePV effect shows unique characteristics, such as ultrafast spontaneous photocurrent [42], low noise current [43], and no dissipation [44], the anomalous photovoltaic effect in ferroelectrics is evidently different from conventional photovoltaic effects based on p-n junctions [40,41]. Therefore, the FePV effect has attracted considerable attention in material chemistry and physics. While the FePV effect in ferroelectric ceramics has been widely investigated for several decades [38–44], reports on the FePV effect in organic materials other than the FePV effect of CLCs [16–19,22] are still limited [45–47]. The FePV effect for organic materials is essential for developing novel high-performance organic photoelectronic devices, including organic photovoltaic cells and organic photodetectors [47]. In fact, the FePV effect with a high open-circuit voltage of over 1 V was recently achieved by using CLCs doped with a fullerene derivative [48]. The exploration of CLCs, which are candidates for the active materials of the FePV effect, has only begun and is still important. In particular, tuning the light absorption property is a significant factor in realizing a large short-circuit current density, resulting in efficient charge carrier generation. The most common approach for tuning spectroscopic properties is expanding the π-conjugated systems, such as by introducing an ethynyl linker.

In this study, we examined the influence of the ethynyl linker between oligothiophene and chiral fluorophenyl units on the LC and photophysical properties. In addition, the impact of bilateral symmetry of the chiral compounds upon those properties were studied. We synthesized three chiral π-conjugated compounds, (*R*)-**1**, (*R*)-**2**, and (*R*)-**3** (Figure 1). Molecular packing in the smectic LC phase and its spectroscopic properties were also investigated.

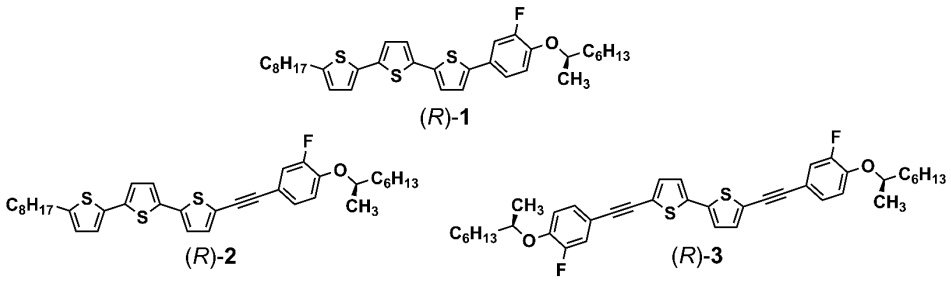

Figure 1. Chemical structures of the chiral π-conjugated compounds (*R*)-**1**, (*R*)-**2**, and (*R*)-**3**.

2. Materials and Methods

2.1. General Procedures and Materials

All reagents were purchased from Sigma-Aldrich Japan (Tokyo, Japan), Tokyo Chemical Industry Co., Ltd.(Tokyo, Japan), Kanto Chemicals (Tokyo, Japan), and FUJIFILM Wako Pure Chemicals (Osaka, Japan) and were used without further purification. All the reactions were performed under an argon atmosphere in a well-dried flask equipped with a magnetic stirring bar. The synthetic scheme for the target compounds is described in the next section (Section 2.2. Synthesis). The details of synthetic conditions are described in the attached Supplementary Files, Section S1. All ^{1}H and ^{13}C NMR spectra were recorded on a Bruker (Osaka, Japan) Biospin AVANCE NEO 400 spectrometer in $CDCl_3$ (400 MHz for ^{1}H NMR spectra, 100 MHz for ^{13}C NMR spectra). All chemical shifts (δ) in the ^{1}H and ^{13}C NMR spectra are quoted in ppm using tetramethylsilane (δ = 0.00) as the internal standard (0.03 vol%). High-resolution mass spectrometry (HRMS) measurements were carried out by electrospray ionization using a SCIEX (Tokyo, Japan) X500R QTOF spectrometer. Elemental analysis was entrusted to A-Rabbit-Science Japan Co., Ltd. (Kanagawa, Japan).

2.2. Synthesis

The chiral π-conjugated compounds (*R*)-**1**, (*R*)-**2**, and (*R*)-**3** were synthesized according to the procedures shown in Scheme 1. All compounds were synthesized via Pd-catalyzed C-C coupling reactions. The chiral starting material (*S*)-2-octanol was purchased from Tokyo Chemical Industry Co., Ltd. (Specification value: chemical purity ≥ 98.0%, optical purity ≥ 98.0%ee). Compounds **4**, (*R*)-**5**, **6**, (*R*)-**7** and **8** were synthesized with reference to literatures [17,19,49–51]. The chiral compound (*R*)-**5** was synthesized via the Suzuki–Miyaura reaction between 2,2′-bithiophene-5-boronic acid pinacol ester and 4-bromo-2-fluoro-1-{(*R*)-2-octyloxy}benzene. 4-Bromo-2-fluoro-1-{(*R*)-2-octyloxy}benzene was synthesized via the Mitsunobu reaction between 4-bromophenol and (*S*)-2-octanol. It is noted that the optical purity of (*S*)-2-octanol is guaranteed ≥ 98.0%ee by the standard. Because the Mitsunobu reaction generally undergoes the typical S_N2 displacement pathway, chiral inversion must be caused [52]. Shi et al. reported that the Mitsunobu reaction using chiral alcohols exhibiting high enantiomeric excess (> 90%ee) with phenol derivatives afford the product with high optical purity (> 90%ee) [53]. Based on these findings, various chiral liquid crystals have been synthesized from (*S*)-2-octanol or (*R*)-2-octanol the several reaction steps including Mitsunobu reaction and C-C cross-coupling reactions [54–57]. ^{1}H-, ^{13}C NMR and HRMS spectra for the target compounds (*R*)-**1**, (*R*)-**2**, and (*R*)-**3** are shown in the ESI, Sections S2 and S3.

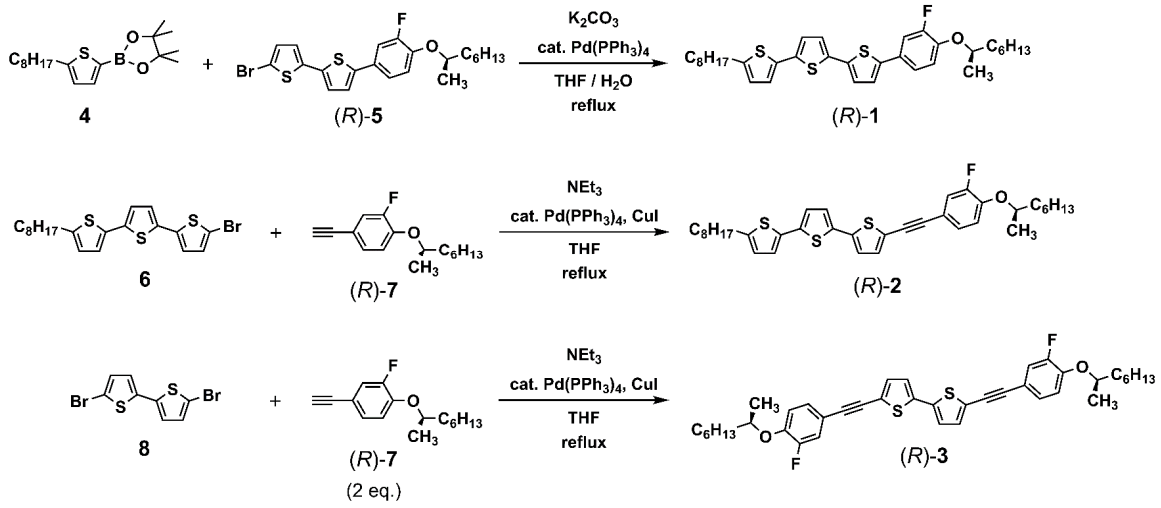

Scheme 1. Synthesis routes of compounds (*R*)-**1**, (*R*)-**2**, and (*R*)-**3**.

2.2.1. Characterization of (*R*)-**1**

5-Octyl-5″-{3-fluoro-4-[(*R*)-2-octyloxy]phenyl}-2,2′:5′,2″-terthiophene: (*R*)-**1**

^{1}H NMR (400 MHz, $CDCl_3$): δ [ppm] = 7.30 (dd, 1H, *J* = 12.2, 2.2 Hz), 7.25 (ddd, 1H, *J* = 8.4, 2.4, 1.2 Hz), 7.10 (d, 1H, *J* = 3.6 Hz), 7.08 (d, 1H, *J* = 3.6 Hz), 7.05 (d, 1H, *J* = 3.6 Hz), 6.99 (d, 1H, *J* = 4.0 Hz), 6.98 (d, 1H, *J* = 3.2 Hz), 6.95 (t, 1H, *J* = 8.6 Hz), 6.68 (d, 1H, *J* = 3.6 Hz), 4.37 (sextet, 1H, *J* = 6.0 Hz), 2.79 (t, 2H, *J* = 7.4 Hz), 1.86–1.55 (m, 4H), 1.51–1.20 (m, 18H), 1.33 (d, 3H, *J* = 6.0 Hz), 0.89 (t, 6H, *J* = 7.0 Hz); ^{13}C NMR (100 MHz, $CDCl_3$): δ [ppm] = 153.8 (d, *J* = 244.2 Hz), 145.8 (d, *J* = 10.9 Hz), 145.7, 141.8 (d, *J* = 2.2 Hz), 136.9, 136.3, 135.4, 134.4, 127.8 (d, *J* = 7.2 Hz), 124.9, 124.3, 124.1, 123.5 (d, *J* = 15.9 Hz), 123.4, 121.4 (d, *J* = 3.6 Hz), 117.9 (d, *J* = 2.7 Hz), 113.8, 113.6, 76.6, 36.5, 31.9, 31.8, 31.6, 30.2, 29.3, 29.3, 29.2, 29.1, 25.4, 22.7, 22.6, 19.8, 14.1, 14.1; HRMS (ESI): molecular weight: 582.8954 ($C_{34}H_{43}FOS_3$); m/z calculated for $[C_{34}H_{43}FOS_3]^+$: 582.2455 ($[M]^+$); found: 582.2456; elemental analysis (%) calculated for $C_{34}H_{43}FOS_3$: C 70.06, H 7.44, F 3.26, O 2.74, S 16.50; found: C 69.81, H 7.28.

2.2.2. Characterization of (*R*)-**2**

5-Octyl-5″-({3-fluoro-4-[(*R*)-2-octyloxy]phenyl}ethynyl)-2,2′:5′,2″-terthiophene: (*R*)-**2**

^{1}H NMR (400 MHz, $CDCl_3$): δ [ppm] = 7.25–7.18 (m, 2H), 7.14 (d, 2H, *J* = 3.6 Hz), 7.07 (d, 1H, *J* = 4.0 Hz), 7.03 (d, 1H, *J* = 4.0 Hz), 6.99 (d, 1H, *J* = 4.0 Hz), 6.99 (d, 1H, *J* = 3.6 Hz), 6.91 (t, 1H, *J* = 8.8 Hz), 4.39 (sextet, 1H, *J* = 6.0 Hz), 2.79 (t, 2H, *J* = 7.6 Hz), 1.85–1.55 (m, 4H), 1.52–1.22 (m, 18H), 1.33 (d, 3H, J = 6.4 Hz), 0.88 (t, 6H, *J* = 6.8 Hz); ^{13}C NMR (100 MHz, $CDCl_3$): δ [ppm] = 152.9 (d, *J* = 244.8 Hz), 147.0 (d, *J* = 10.9 Hz), 146.0, 138.7, 137.6, 134.7, 134.2, 132.7, 127.9 (d, *J* = 3.6 Hz), 124.9, 124.8, 123.6 (d, *J* = 3.2 Hz), 123.2, 121.7, 119.4, 119.2, 116.7 (d, *J* = 2.4 Hz), 115.3 (d, *J* = 8.3 Hz), 93.2, 82.0, 76.3, 36.4, 31.9, 31.8, 31.6, 30.2, 29.3, 29.2, 29.1, 25.4, 22.7, 22.6, 19.8, 14.1, 14.1; HRMS (ESI): molecular weight: 606.9174 ($C_{36}H_{43}FOS_3$); m/z calculated for $[C_{36}H_{43}FOS_3]^+$: 606.2455 ($[M]^+$); found: 606.2453; elemental analysis (%) calculated for $C_{36}H_{43}FOS_3$: C 71.24, H 7.14, F 3.13, O 2.64, S 15.85; found: C 71.25, H 7.16.

2.2.3. Characterization of (*R*)-**3**

5,5′-Bis({3-fluoro-4-[(*R*)-2-octyloxy]phenyl}ethynyl)-2,2′-bithiophene: (*R*)-**3**

^{1}H NMR (400 MHz, $CDCl_3$): δ [ppm] = 7.25–7.19 (m, 4H), 7.15 (d, 2H, *J* = 3.6 Hz), 7.07 (d, 2H, *J* = 4.0 Hz), 6.92 (t, 2H, *J* = 8.6 Hz), 4.40 (sextet, 2H, *J* = 6.2 Hz), 1.85–1.72 (m, 2H), 1.67–1.55 (m, 2H), 1.52–1.24 (m, 16H), 1.33 (d, 6H, *J* = 6.4 Hz), 0.88 (t, 6H, *J* = 6.8 Hz); ^{13}C NMR (100 MHz, $CDCl_3$): δ [ppm] = 152.9 (d, *J* = 245.4 Hz), 147.1 (d, *J* = 10.8 Hz), 138.0, 132.7, 128.0 (d, *J* = 3.0 Hz), 124.0, 122.5, 119.3 (d, *J* = 20.2 Hz), 116.7 (d, *J* = 2.4 Hz), 115.2 (d, *J* = 8.5 Hz), 93.5 (d, *J* = 2.8 Hz), 81.8, 76.3, 36.4, 31.8, 29.2, 25.4, 22.6, 19.8, 14.1; HRMS (ESI): molecular weight: 658.9068 ($C_{40}H_{44}F_2O_2S_2$); m/z calculated for $[C_{40}H_{45}F_2O_2S_2]^+$: 659.2824 ($[M+H]^+$); found: 659.2828; elemental analysis (%) calculated for $C_{40}H_{44}F_2O_2S_2$: C 72.91, H 6.73, F 5.77, O 4.86, S 9.73; found: C 72.99, H 6.86.

2.3. Characterization of LC Properties

The LC properties of chiral π-conjugated compounds were characterized using differential scanning calorimetry (DSC), polarizing optical microscopy (POM), and X-ray diffraction (XRD). DSC measurements were conducted using a SHIMADZU (Kyoto, Japan) DSC-60 system equipped with a liquid nitrogen auto-cooling system (TAC-60L). Approximately 2–3 mg of each sample was sealed in an aluminum pan. The optical texture was observed using a polarizing optical microscope (Olympus BH2, Olympus Corporation, Tokyo, Japan) equipped with a digital camera (AS ONE HDCE-X1 (AS ONE Corporation, Osaka, Japan) and a temperature control system (METTLER TOLEDO FP90 and FP82HT). Indium tin oxide (ITO) sandwich cells filled with chiral π-conjugated compounds were used for POM observations. Empty ITO sandwich cells (KSSO-02/A311P1NSS05, cell gap: 2 μm) were purchased from EHC Corporation (Tokyo, Japan). The ITO surface without a polyimide was rubbed to assist in the planar orientation of the smectic phases. The scan rate of DSC measurements and POM observations was 10 °C min^{-1}. XRD measurements were performed using a Rigaku RINT-2500 (Ni-filtered Cu Kα radiation, Rigaku Corporation,

Tokyo, Japan) equipped with a custom-made thermal control system composed of a silicone rubber heater, thermocouple sensor, and PID-type thermal controller (AS ONE TJA-550).

2.4. Characterization of Spectroscopic Properties

UV–vis absorption spectra were recorded using a JASCO (Tokyo, Japan) V-650 spectrometer. UV-vis absorption spectra were measured using a pair of quartz cells (cell gap: 1 cm). The photoluminescence (PL) emission spectra were recorded using a SHIMADZU (Kyoto, Japan) RF-6000 spectrometer. Emission spectra were measured using a pair of quartz cells (cell gap: 1 cm).

3. Results and Discussion

3.1. Liquid-Crystalline Properties

3.1.1. Polarizing Optical Microscopy

In the POM observation of chiral phenylterthiophene derivative (*R*)-**1**, a broken fan-like texture with stripes was observed in the area where the sample was sandwiched between two ITO electrodes, at approximately 140 °C upon cooling from the isotropic liquid (IL) state (Figure 2a). The broken fan-like domains suggest the formation of an LC tilted-layer structure. Furthermore, the stripe pattern in each fan-shaped domain should be derived from the disclination. Therefore, the characteristic optical textures indicated the appearance of a chiral smectic C (SmC*) phase with a nonpolar helical structure. When the sample was cooled to approximately 130 °C, the polarized optical texture was transformed, and tile-like domains were observed in the homeotropic domains of the SmC* phase between the two glass substrates (Figure 2b). This change in texture corresponds to a phase transition from SmC* to ordered smectic phases. Upon further cooling to room temperature, the domain shapes were maintained without drastic textural changes (Figure 2c). In the POM study of compound (*R*)-**2**, an ethynyl linker introduced between the terthiophene and chiral fluorophenyl units, we observed a fan-shaped texture upon cooling from the IL phase (Figure 3a). A typical fan-shaped texture shows the appearance of a smectic LC phase. Because the color and contrast of the optical texture vary as the sample temperature of (*R*)-**2** decreases to approximately 110 °C (Figure 3b), the high-temperature smectic LC phase is changed to another smectic LC phase at this temperature. After cooling below 100 °C, the stripes appeared in fan-shaped domains (Figure 3c). In the polarized optical texture of (*R*)-**2** at 45 °C, the stripes of fan-shaped domains are more conspicuous (Figure 3d). The slight change of optical texture is probably due to rearrangements in the intralayer molecular packing. These results support that (*R*)-**2** exhibited several smectic LC phases. In the POM observation of compound (*R*)-**3** modified with chiral fluorophenyl units on both wings of the 2,2′-bithiophene core, two types of optical textures were observed during cooling from the IL phase (Figure 4a,b). However, these textures differ from the distinctive textures of LC phases. Therefore, we conclude that (*R*)-**3** does not exhibit LC properties.

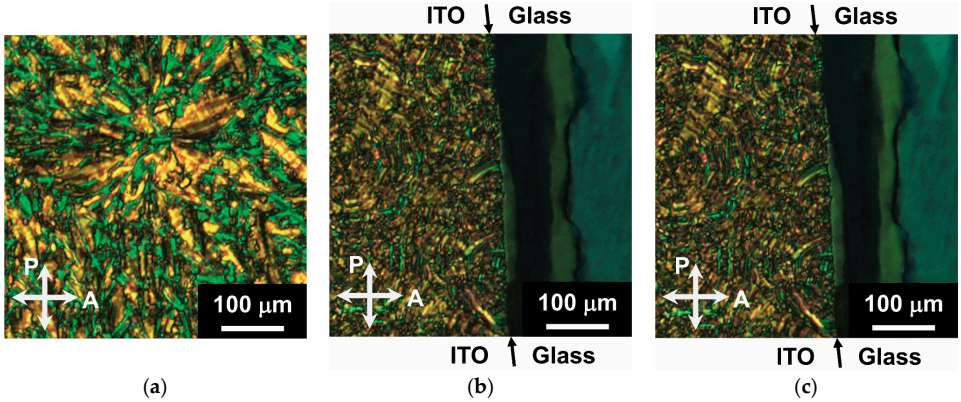

Figure 2. POM images of (*R*)-**1** at (**a**) 140 °C, (**b**) 95 °C, and (**c**) 40 °C. The black arrows indicate the border of ITO electrode and glass surface.

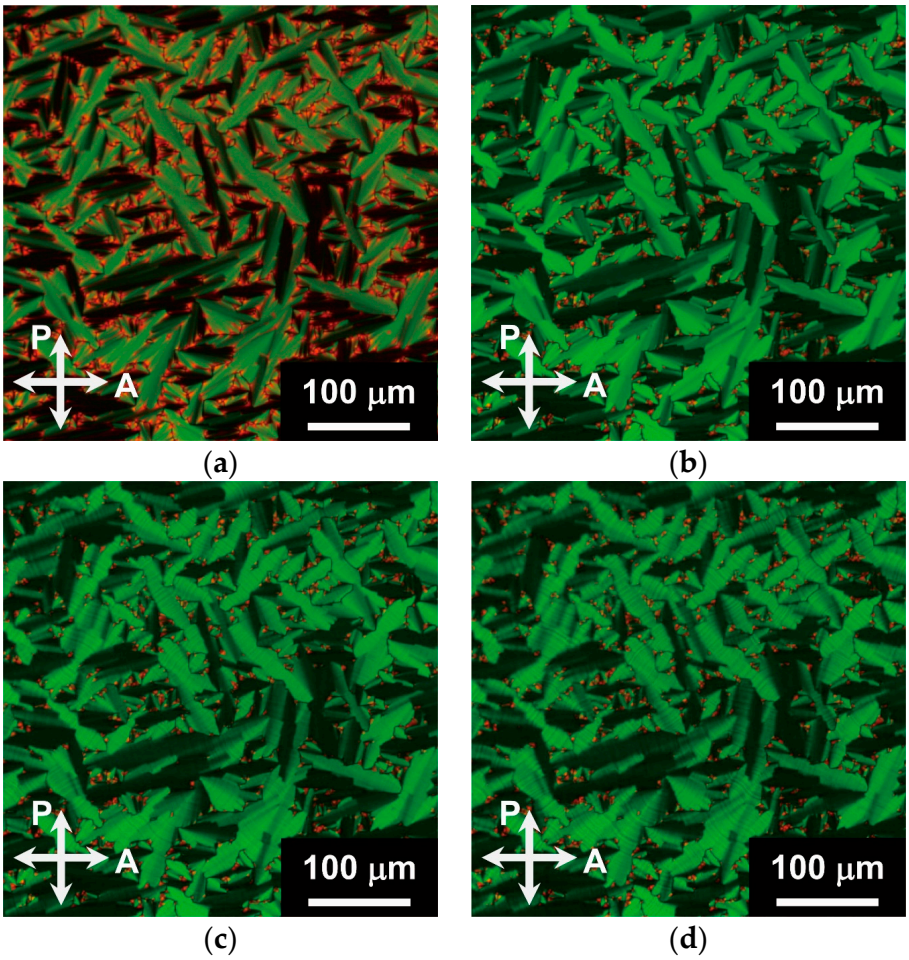

Figure 3. POM images of (*R*)-**2** at (**a**) 120 °C, (**b**) 105 °C, (**c**) 90 °C, and (**d**) 45 °C.

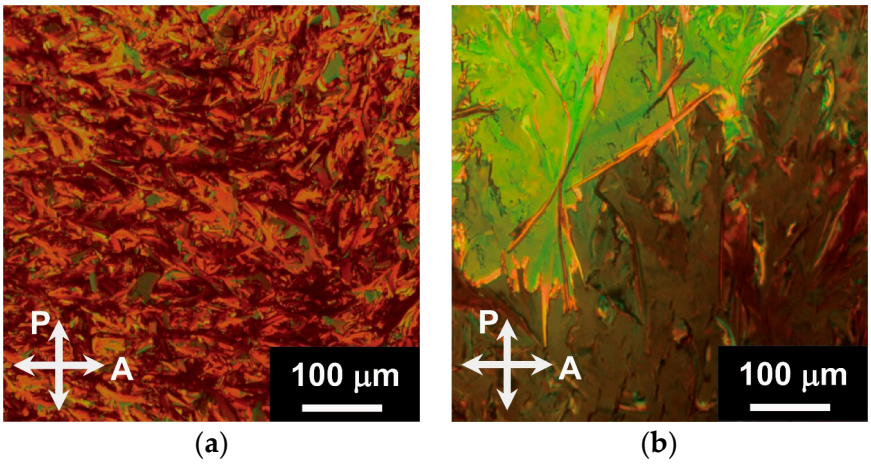

Figure 4. POM images of (*R*)-**3** at (**a**) 70 °C, and (**b**) 40 °C.

3.1.2. Differential Scanning Calorimetry

The DSC thermogram of (*R*)-**1** exhibits two distinct endothermic peaks due to first-order phase transitions during the second heating (Figure 5a). Although a crystal-LC phase transition peak is found at 63.3 °C on the first heating, no endothermic peak of crystal-LC transition is seen on subsequent heating scans. Similar phase transition behaviors are found in analogous phenylterthiophene derivatives [17,37]. The inconsistency in the number of first-order phase transition peaks between first cooling and second heating scans

suggests the existence of a monotropic metastable mesophase during cooling. When we consider the results of POM and DSC studies of (*R*)-**1**, the exothermic peak at 144.2 °C during cooling indicates the IL–SmC* phase transition. The following peak observed at 131.3 °C corresponds to the transition from SmC* to metastable ordered smectic phases. The metastable smectic phase transforms to a more stable ordered smectic phase at 66.5 °C during cooling. On the second heating scan, the endothermic peak of the ordered smectic-SmC* phase transition is observed at 132.5 °C, and the SmC*-IL phase transition follows at 144.8 °C. In the DSC thermogram of (*R*)-**2**, three peaks are observed during the second heating (Figure 5b). These peaks correspond to the two LC–LC phase transitions and an LC–IL phase transition based on the results of the POM study. The middle LC phase changes to the low-ordered smectic phase at 111.5 °C after the first LC–LC phase transition occurs at 101.3 °C. The smectic LC structure and the molecular order collapses at 126.0 °C. The broad exothermic peak, at approximately 67 °C, is observed on the first cooling scan, corresponding to the transition from metastable to stable states (Figure 5b). A metastable LC phase is observed during cooling for compound (*R*)-**2**. Therefore, we conclude that compounds (*R*)-**1** and (*R*)-**2** exhibit similar monotropic behavior. The broad tolerance of molecular packing style in (*R*)-**2** should be also reflected to the complicated phase transition behaviors on the first heating process. Compound (*R*)-**3** also shows several phase transitions at 52.3 and 77.2 °C, as observed in the second heating scan (Figure 5c). The DSC and POM studies support that compound (*R*)-**3** exhibits crystalline polymorphism.

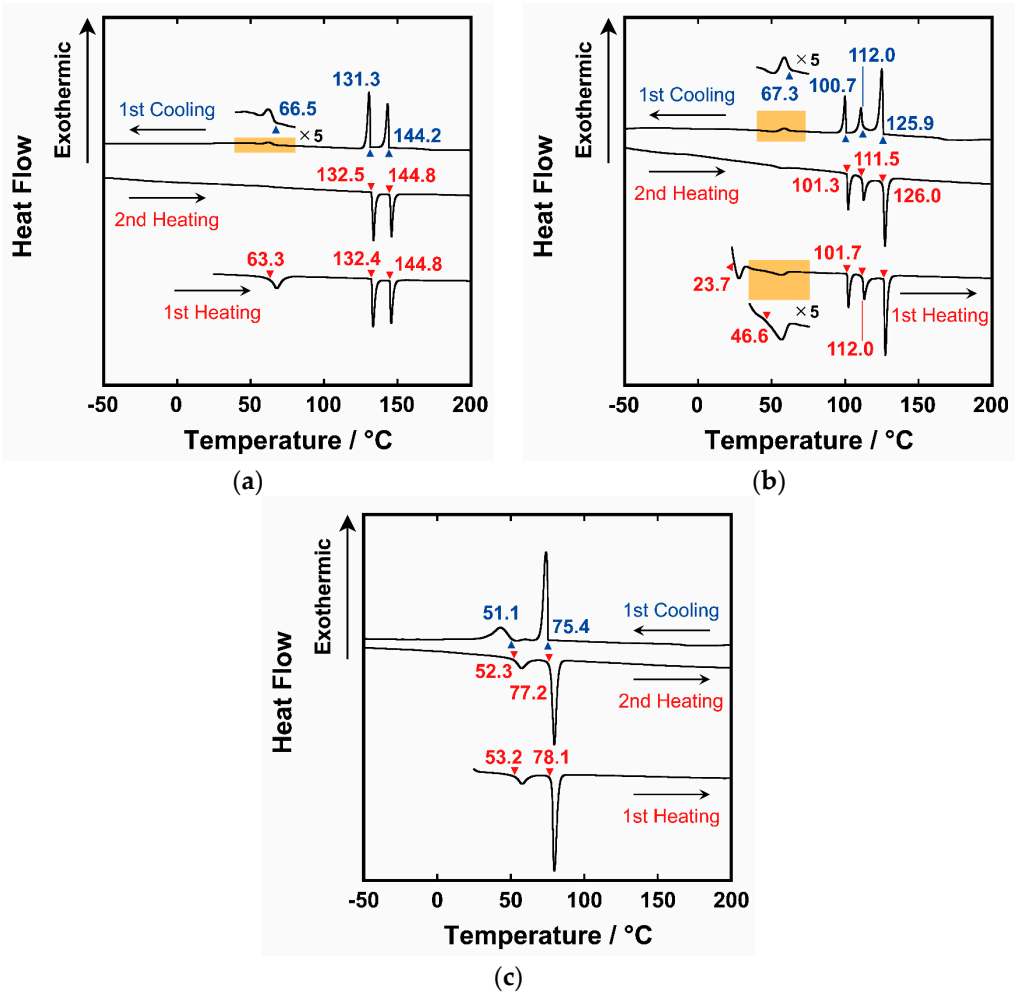

Figure 5. DSC thermograms of (**a**) (*R*)-**1**, (**b**) (*R*)-**2**, and (**c**) (*R*)-**3** at a scanning rate of 10 °C min^{-1}.

3.1.3. X-ray Diffraction

The variable-temperature XRD measurements were conducted for the chiral π-conjugated compounds (*R*)-**1**, (*R*)-**2**, and (*R*)-**3** to gain insight into their molecular packing and self-assembled structures. The XRD pattern of (*R*)-**1** in the SmC* phase at 139 °C (Figure 6a, upper) exhibits diffraction peaks at 2θ = 3.12°, 6.10°, 12.11°, 15.15°, and 18.21°, which correspond to diffractions from the (001), (002), (003), (004), (005), and (006) planes, respectively. Because all *d*-spacings estimated from these diffractions can be expressed as integer ratios, the XRD pattern also indicates that a smectic-layer structure at approximately 140 °C can be formed. The molecules in the smectic-layer structure should be tilted with respect to the normal of the layer because the layer spacing (29 Å) is shorter than the theoretical extended molecular length (35 Å) of (*R*)-**1** estimated by the molecular mechanics calculation (Energy minimization calculation, MM2 force field, PerkinElmer, Chem3D 18.1). The SmC* phase is observed between 144 and 131 °C upon cooling of (*R*)-**1**. This observation coincides with those of the preceding POM and DSC studies. In the XRD pattern, during cooling, we observed a diffraction peak with a low intensity at 95 °C in the wide-angle region (2θ = 19.30°) and several other diffraction peaks that represented from the smectic-layer structures (Figure 6a, middle). The low-intensity peak can be assigned to the (010) plane, reflecting the intralayer order. From the periodic diffraction peaks corresponding to the (001), (002), (003), (004), and (006) planes, the layer spacing is estimated to be 29 Å. Therefore, the tilt angle remains unchanged through the SmC*–LC phase transition. As no other peaks are observed in the wide-angle region, the intralayer order in the metastable smectic phase should be confined in the short range. Therefore, we consider the metastable phase at 95 °C to be an ordered chiral smectic (SmX_1*) phase which is probably either chiral smectic F or chiral smectic I phase [57–60]. The XRD profile of the more stable highly ordered chiral smectic (SmX_2*) phase at 27 °C differed from those of the SmC* and SmX_1* phases (Figure 6a, lower). The increase in the intralayer molecular order is indicated by a broad peak observed at 2θ = 18.64° for the (100) plane and by an increase in the relative peak intensity of the (010) diffraction. The shorter layer spacing of 29 Å and the calculated molecular length indicate that the tilted-layer structure is maintained even in the ordered smectic phase. This ordered smectic (SmX_2*) phase should be one of the chiral smectic G, chiral smectic J or chiral smectic H phase, as determined by the general phase transition sequence [57–61].

The XRD pattern of the LC phase of (*R*)-**2** at 124 °C (Figure 6b, upper) exhibits several peaks at 2θ = 2.16°, 4.36°, and 6.49°. These three peaks are attributed to the (001), (002), and (003) planes with diffractions derived from the periodicity of the smectic-layer structure. Although the extended molecular length of (*R*)-**2** is estimated to be 38 Å by MM2 calculations, the experimentally obtained layer spacing is 41 Å. The layer spacing is greater than the theoretical molecular length that an interdigitated layer structure can achieve. The halos observed at approximately 2θ = 12°, 20°, 24°, and 26° also confirm the interdigitated organization of (*R*)-**2** molecules. Because the POM textures of (*R*)-**2** at a comparable temperature are typical for a low-ordered smectic phase and not for a characteristic texture for a highly ordered smectic phase, the formation of a highly ordered smectic phase is uncertain. In addition, the sample of (*R*)-**2** shows fluidity in the LC phase. These behaviors can be observed in a low-ordered interdigitated smectic phase. While the halo at 2θ = 12° can be ascribed to the disordered aggregation of bulky chiral alkyl chains based on steric effects, the series of halos between 2θ = 18° and 2θ = 30° probably resulted from the disordered aggregation of the linear aliphatic chains and interaction between aromatic units. Thus, the appearance of several halos suggests that each of the rigid aromatic units and mobile chiral alkyl chains is segregated and gathered in different periodicities. The integrated molecules of (*R*)-**2** in the LC phase should be tilted with respect to the layer normal, considering the molecular packing model (Figure 7). Therefore, upon cooling, we assigned the LC phase of (*R*)-**2** between 126 °C and 112 °C to an interdigitated chiral smectic C (SmC_d*) phase [62–67]. When the XRD sample of (*R*)-**2** was cooled to 108 °C, the normalized intensities of the (002) and (003) diffraction peaks in the XRD profile (Figure 6b, middle) were higher than those of the same peaks in the XRD pattern of the

SmC_d* phase (Figure 6b, upper). The absence of sharp diffraction peaks in the wide-angle region indicates the absence of long-range intralayer order in the middle-temperature LC phase. Because the interlayer spacing undergoes a slight change of 41–42 Å via the SmC_d*–LC phase transition, the interdigitated layer structure is maintained. Based on these results, we believe that the middle-temperature LC phase is a chiral smectic (SmX_{d1}*) phase, in which the interdigitated LC structures have short-range intralayer order. In the XRD pattern of (*R*)-**2** cooled to room temperature (34 °C), additional weak diffraction peaks were observed at 2θ = 10.6° and 19.4° (Figure 6b, bottom). These peaks originated from the (005) and (010) diffraction planes. Because the sharp (010) diffraction peak indicates growing intralayer-bond order, the room-temperature LC phase is identified as a highly ordered interdigitated chiral smectic (SmX_{d2}*) phase. The small difference of XRD patterns between SmX_{d1}* phase and SmX_{d2}* phase suggests the slight structural change through phase transitions via the metastable state. The POM study of (*R*)-**2** on cooling process (Figure 3b–d) also supports this consideration. The metastable phase of (*R*)-**2** probably appears while the rearrangement of intralayer molecular packing proceeds under the influence of spatial factors by bulky chiral unit and sparse ethynyl moiety.

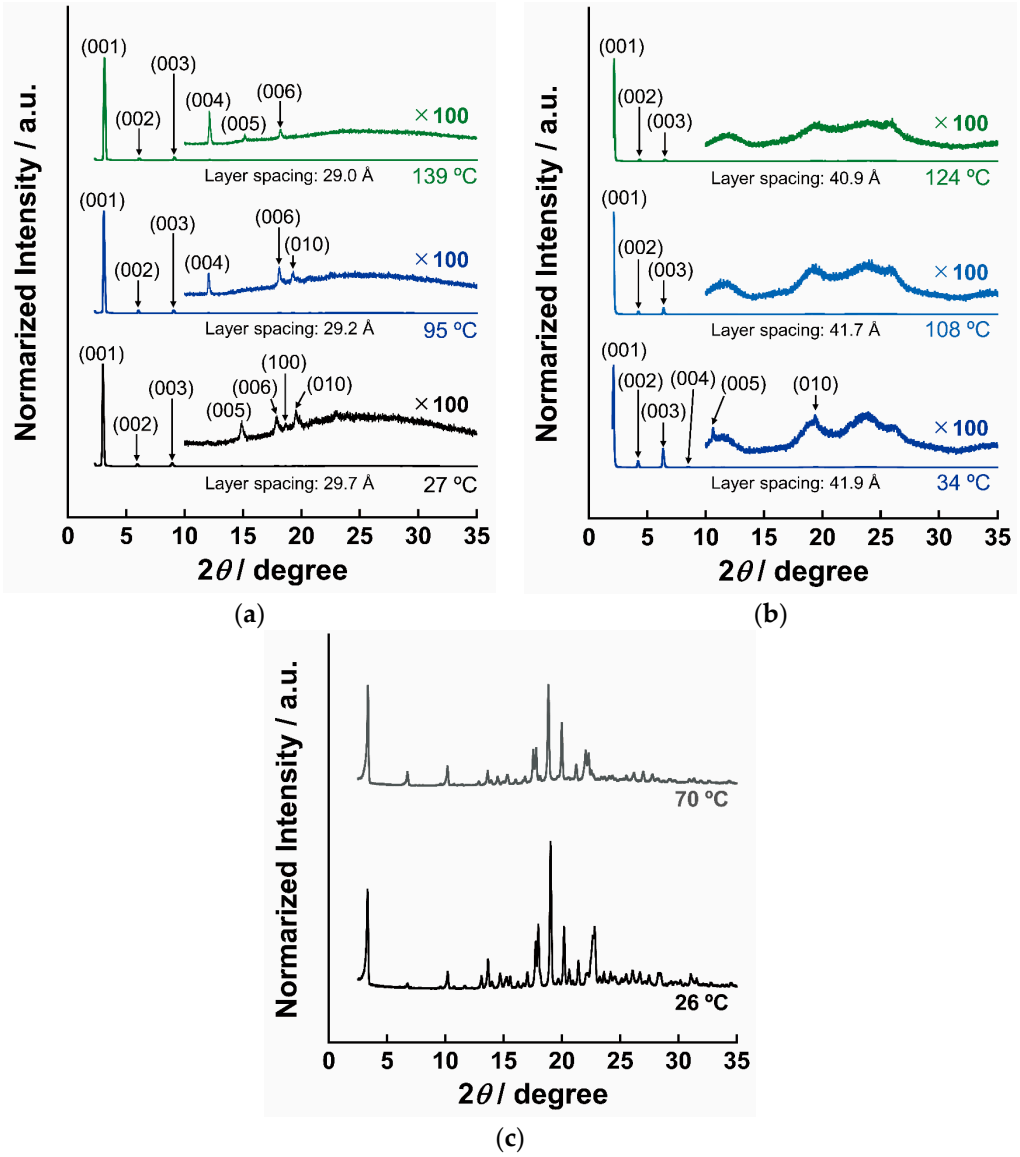

Figure 6. Variable-temperature XRD profiles of (**a**) (*R*)-**1**, (**b**) (*R*)-**2**, and (**c**) (*R*)-**3**.

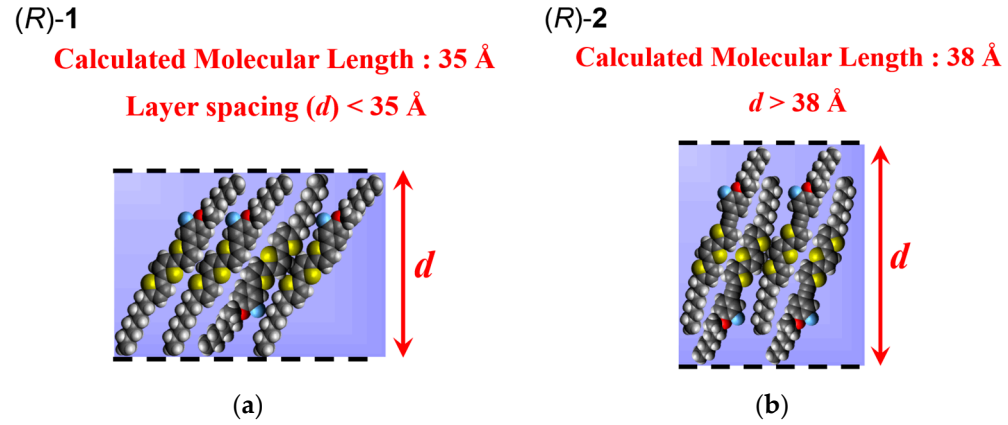

Figure 7. Schematic illustrations of the molecular packing models in the (**a**) SmC* phase of (*R*)-**1** (monolayer structure), and (**b**) SmC_d* phase of (*R*)-**2** (interdigitated layer structure) assumed from the XRD profiles.

Compound (*R*)-**3** exhibited complicated XRD patterns, indicating crystalline molecular packing below 74 °C (Figure 6c). Although several phase transition peaks were observed in the DSC thermogram, bis({fluorophenyl}ethynyl) bithiophene (*R*)-**3** showed crystal polymorphism and did not show any thermodynamically stable LC phase.

The phase transition behaviors of (*R*)-**1**, (*R*)-**2**, and (*R*)-**3** are summarized in Table 1. For each of LC compounds (*R*)-**1** and (*R*)-**2**, the initial crystalline precipitates for the characterization of LC properties were obtained by recrystallization. It is noted that both LC compounds (*R*)-**1** and (*R*)-**2** exhibit the crystalline–LC phase transition only in the first heating process. Once the precipitates melted to the IL phase, no crystallization occurred during the cooling process below −50 °C at a scanning rate of 10 °C min^{-1}. These results show that a bilateral asymmetric molecular structure is effective for liquid crystallinity. In addition, we consider that the interplay of bulky chiral unit and sparse ethynyl moiety prominently causes a variety of molecular packing as well as the formation of interdigitated structures.

Table 1. Phase transition behavior of (*R*)-**1**, (*R*)-**2**, and (*R*)-**3**.

Compound		Phase Transition Temperature/°C (Enthalpy/kJ mol^{-1})
(*R*)-**1**	first heating	Cr 63 (−13) SmX_2* 132 (−13) SmC* 145 (−11) IL
	first cooling	IL 144 (11) SmC* 131 (12) SmX_1* 67 (1) SmX_2*
	second heating	SmX_2* 133 (−13) SmC* 145 (−11) IL
(*R*)-**2**	first heating	Cr 24 (−5) M 47 (−2) SmX_{d2}* 102 (−3) SmX_{d1}* 112 (−4) SmC_d* 126 (−9) IL
	first cooling	IL 126 (9) SmC_d* 112 (3) SmX_{d1}* 101 (4) SmX_m* 67 (1) SmX_{d2}*
	second heating	SmX_{d2}* 101 (−3) SmX_{d1}* 112 (−3) SmC_d* 126 (−8) IL
(*R*)-**3**	first heating	Cr_2 53 (−9) Cr_1 78 (−37) IL
	first cooling	IL 75 (33) Cr_1 51 (18) Cr_2
	second heating	Cr_2 52 (−9) Cr_1 77 (−36) IL

The abbreviations Cr, Cr_1, Cr_2, IL, M, SmC*, SmC_d*, SmX_1*, SmX_2*, SmX_{d1}*, SmX_{d2}*, and SmX_m* denote crystalline, crystalline 1, crystalline 2, isotropic liquid, unidentified ordered, chiral smectic C, chiral interdigitated smectic C, unidentified ordered chiral smectic 1, unidentified ordered chiral smectic 2, unidentified interdigitated ordered smectic 1, interdigitated ordered smectic 2, and metastable interdigitated ordered smectic phases, respectively.

3.2. Spectroscopic Properties

Figure 8a shows the UV–vis absorption and PL spectra in a dilute THF solution of (*R*)-**1**, (*R*)-**2**, and (*R*)-**3**. The absorption spectrum of (*R*)-**1** in THF (10 μM) showed a quasi-unimodal absorption band corresponding to the π–π* transition of the terthiophene unit between 330 and 450 nm. The absorption maximum was 393 nm with a molar absorption coefficient of 4.0×10^4 L mol^{-1} cm^{-1}. By comparing the absorption spectra of (*R*)-**1** and

(*R*)-**2** in THF dilute solutions, a slight shift in the absorption band of (*R*)-**2** is observed towards the longer wavelength region. This result suggested that introducing an ethynyl linker to the mesogenic core accurately extended the effective π-conjugation length. In addition, the THF solution of compound (*R*)-**2** showed a higher molar absorption coefficient of 4.7×10^4 L mol^{-1} cm^{-1} at the absorption maximum (λ_{abs} = 397 nm) compared to those of the solution of (*R*)-**1**. The absorption spectrum of (*R*)-**3** in THF (10 μM) displays the π–π * transition band of the bithiophene core with an absorption maximum of 390 nm. For a dilute solution of (*R*)-**3**, the molar absorption coefficient attained 5.5×10^4 L mol^{-1} cm^{-1}. The absorption edges in the THF solutions of (*R*)-**1**, (*R*)-**2,** and (*R*)-**3** are 446, 450, and 455 nm, respectively (Figure 8b). Because the order of the absorption maxima and edges reflects the π-conjugation length, (*R*)-**2** should have the longest effective π-conjugation length among the three compounds. Each fluorescence spectrum indicates well-resolved vibrational structures (Figure 8a). The maximum PL intensity of (*R*)-**3** in the THF solution was more than twice those of (*R*)-**1** and (*R*)-**2**. This result indicates that modifying phenylethynyl units on both wings of the 2,2′-bithiophene core enhances fluorescence emission. The luminescence enhancement appears to result from the suppression of thermal relaxation, and an increase in the oscillator strength is observed. In the case of compound (*R*)-**3**, introducing an ethynyl linker may reduce steric interactions and extend the π-conjugation length [68]. Table 2 lists the spectroscopic parameters. The disubstituted compound (*R*)-**3** showed the slightest Stokes shift among the three compounds, and phenylethynyl terthiophene (*R*)-**2** displayed the most significant Stokes shift. According to previous reports, we considered that the difference in Stokes shift originated from conformational changes rather than solvent effects [68]. The difference in Stokes shift implies a variation in the conformational change between the ground and excited states. The modification of the chiral phenylethynyl units showed different effects on excitation and emission in (*R*)-**3** and (*R*)-**2**. Because interorbital electronic interactions are sensitive to modifications, the principal cause of the difference in spectroscopic properties of (*R*)-**2** and (*R*)-**3** seems to be left-right asymmetrical hetero-substitution. The lack of a drastic increase in the PL intensity of (*R*)-**2** also supports this hypothesis.

Table 2. Spectroscopic properties of (*R*)-**1**, (*R*)-**2**, and (*R*)-**3** in a dilute THF solution (10 μM).

Compound	λ_{abs}/nm (Molar Absorption Coefficient/L mol^{-1} cm^{-1})	λ_{em}/nm	Stokes Shift/eV
(*R*)-**1**	393 (4.0×10^4)	451, 478 [a]	0.406
(*R*)-**2**	397 (4.7×10^4)	458, 483 [b]	0.416
(*R*)-**3**	390 (5.5×10^4)	445, 471 [c]	0.393

[a] Excitation wavelength of 393 nm. [b] Excitation wavelength: 397 nm. [c] The excitation wavelength was 390 nm.

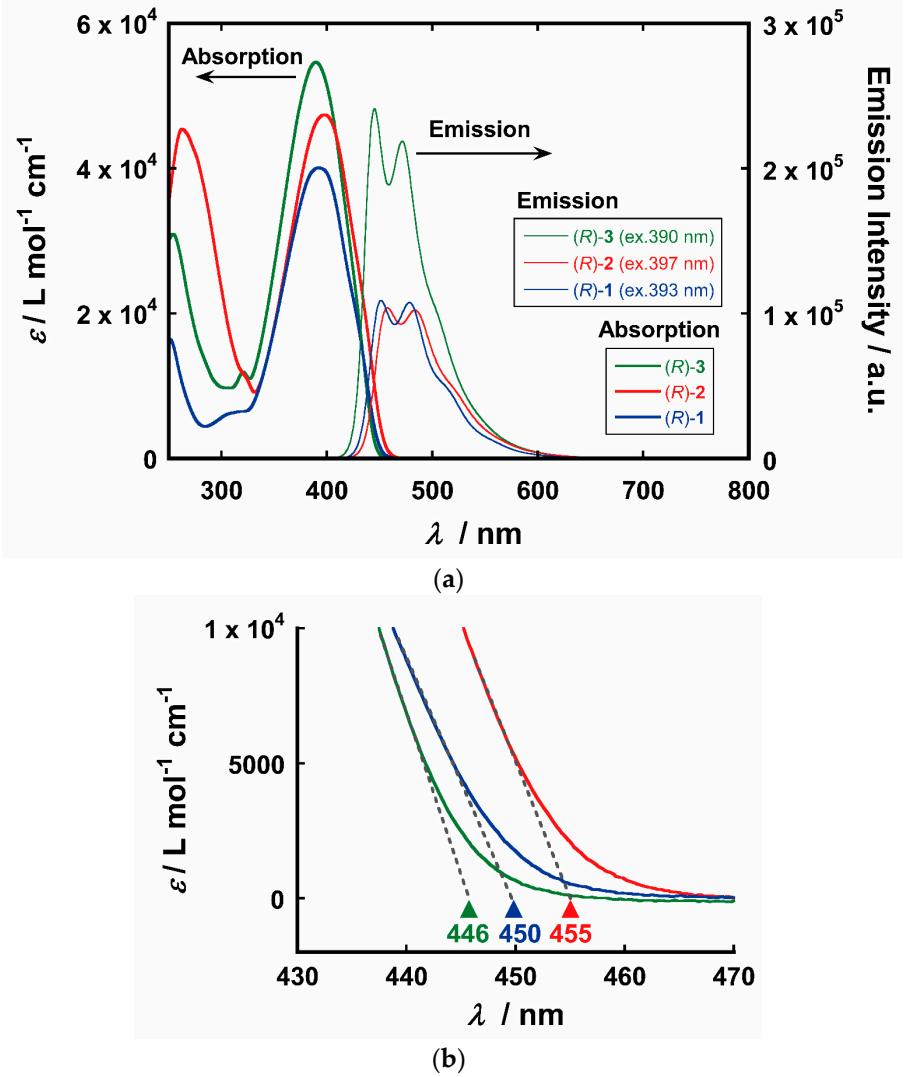

Figure 8. (**a**) UV–vis absorption and photoluminescent spectra in THF dilute solution (10 μM) of (*R*)-**1**, (*R*)-**2**, and (*R*)-**3**. (**b**) The magnified UV–vis absorption spectra in (**a**). Each triangle marks in the inset of absorption spectra depicting the absorption edge of (*R*)-**1** (blue), (*R*)-**2** (red), and (*R*)-**3** (green).

4. Conclusions

We synthesized three chiral oligo-thiophene derivatives, (*R*)-**1**, (*R*)-**2**, and (*R*)-**3**. While compounds (*R*)-**1** and (*R*)-**2** exhibited chiral smectic LC phases, the disubstituted bithiophene analog (*R*)-**3** showed only crystalline polymorphism. This outcome suggests that the bilateral symmetry hinders liquid-crystallinity. In other words, molecular structuring with left-right asymmetry promotes the formation of LC structures. The ethynyl-inserted monosubstituted compound (*R*)-**2** forms LC interdigitated layer structures due to the steric effect of the spatially sparse ethynyl linker and the bulky chiral moiety. In addition, the interplay of both units could effectively contribute to the formation of various smectic LC structures. The UV–vis absorption and PL spectra in a dilute THF solution indicate that (*R*)-**2** has a more expansive π-conjugation system than (*R*)-**1** because of the introduction of the ethynyl linker. The ethynyl linker also contributed to an increase in the molar absorption coefficient in the visible region. Because the molecular packing and photophysical properties affect the photoconductive properties, introducing an ethynyl linker in the central π-conjugated core causes drastic changes in the performance of organic optoelectronic devices. We believe our results can help in the molecular design of novel functional chiral π-conjugated liquid crystals, including ferroelectric π-conjugated liquid crystals that exhibit the FePV effect.

Supplementary Materials: The following supporting information can be downloaded from https://www.mdpi.com/article/10.3390/cryst12091278/s1, Section S1. Synthetic procedure; Section S2. ^{1}H and ^{13}C NMR spectra (Figure S1. ^{1}H NMR spectrum of (*R*)-**1**; Figure S2. ^{13}C NMR spectrum of (*R*)-**1**; Figure S3. ^{1}H NMR spectrum of (*R*)-**2**; Figure S4. ^{13}C NMR spectrum of (*R*)-**2**; Figure S5. ^{1}H NMR spectrum of (*R*)-**3**; Figure S6. ^{13}C NMR spectrum of (*R*)-**3**); Section S3. High-resolution electrospray ionization (ESI) mass spectra (Figure S7. High-resolution ESI mass spectrum of (*R*)-**1**; Figure S8. High-resolution ESI mass spectrum of (*R*)-**2**; Figure S9. The high-resolution ESI mass spectrum of (*R*)-**3**).

Author Contributions: Conceptualization, A.S.; methodology, A.S.; validation, A.S., K.S. and K.A.; formal analysis, A.S. and K.S.; investigation, A.S. and K.S.; resources, A.S. and K.A.; data curation, A.S. and K.S.; writing—original draft preparation, A.S.; writing—review and editing, A.S. and K.S.; visualization, A.S. and K.S.; supervision, A.S. and K.A.; project administration, A.S.; funding acquisition, A.S. and K.A. All authors have read and agreed to the published version of the manuscript.

Funding: This study was financially supported by a research fund from the Tokyo University of Science for A.S. and K.A. and a research grant from the Amano Institute of Technology, Japan for A.S.

Institutional Review Board Statement: Not applicable.

Informed Consent Statement: Not applicable.

Data Availability Statement: Not applicable.

Acknowledgments: The authors thank Khoa V. Le and T. Sasaki at the Tokyo University of Science for their help with POM observations. We also greatly appreciate the help of HRMS measurements by Y. Yoshimura at the Tokyo University of Science.

Conflicts of Interest: The authors declare no conflict of interest.

References

1. Kasprzyk-Hordern, B. Pharmacologically active compounds in the environment and their chirality. *Chem. Soc. Rev.* **2010**, *39*, 4466–4503. [CrossRef] [PubMed]
2. Bisoyi, H.K.; Li, Q. Light-Directing Chiral Liquid Crystal Nanostructures: From 1D to 3D. *Acc. Chem. Res.* **2014**, *47*, 3184–3195. [CrossRef] [PubMed]
3. Pescitelli, G.; Di Bari, L.; Berova, N. Application of electronic circular dichroism in the study of supramolecular systems. *Chem. Soc. Rev.* **2014**, *43*, 5211–5233. [CrossRef] [PubMed]
4. Zhang, L.; Qin, L.; Wang, X.; Cao, H.; Liu, M. Supramolecular Chirality in Self-Assembled Soft Materials: Regulation of Chiral Nanostructures and Chiral Functions. *Adv. Mater.* **2014**, *26*, 6959–6964. [CrossRef] [PubMed]
5. Zhang, L.; Wang, T.; Shen, Z.; Liu, M. Chiral Nanoarchitectonics: Towards the Design, Self-Assembly, and Function of Nanoscale Chiral Twists and Helices. *Adv. Mater.* **2016**, *28*, 1044–1059. [CrossRef]
6. Yashima, E.; Ousaka, N.; Taura, D.; Shimomura, K.; Ikai, T.; Maeda, K. Supramolecular Helical Systems: Helical Assemblies of Small Molecules, Foldamers, and Polymers with Chiral Amplification and Their Functions. *Chem. Rev.* **2016**, *116*, 13752–13990. [CrossRef]
7. Evers, F.; Aharony, A.; Bar-Gill, N.; Entin-Wohlman, O.; Hedegaard, P.; Hod, O.; Jelinek, P.; Kamieniarz, G.; Lemeshko, M.; Michaeli, K.; et al. Theory of Chirality Induced Spin Selectivity: Progress and Challenges. *Adv. Mater.* **2022**, *34*, 2106629. [CrossRef]
8. Meyer, R.B.; Libert, L.; Strzelecki, L.; Keller, P. Ferroelectric liquid crystals. *J. Phys.* **1975**, *36*, L69–L71. [CrossRef]
9. Young, C.Y.; Pindak, R.; Clark, N.A.; Meyer, R.B. Light-Scattering Study of Two-Dimensional Molecular-Orientation Fluctuations in a Freely Suspended Ferroelectric Liquid-Crystal Film. *Phys. Rev. Lett.* **1978**, *40*, 773–776. [CrossRef]
10. Gao, W.; Zhang, Z.; Li, P.F.; Tang, Y.Y.; Xiong, R.G.; Yuan, G.; Ren, S. Chiral Molecular Ferroelectrics with Polarized Optical Effect and Electroresistive Switching. *ACS Nano* **2017**, *11*, 11739–11745. [CrossRef]
11. Scanga, R.A.; Reuther, J.F. Helical polymer self-assembly and chiral nanostructure formation. *Polym. Chem.* **2021**, *12*, 1857–1897. [CrossRef]
12. Dorca, Y.; Greciano, E.E.; Valera, J.S.; Gomez, R.; Sanchez, L. Hierarchy of Asymmetry in Chiral Supramolecular Polymers: Toward Functional, Helical Supramolecular Structures. *Chem. Eur. J.* **2019**, *25*, 5848–5864. [CrossRef] [PubMed]
13. Dierking, I. Chiral Liquid Crystals: Structures, Phases, Effects. *Symmetry* **2014**, *6*, 444–472. [CrossRef]
14. Kitzerow, H.-S.; Bahr, C. (Eds.) *Chirality in Liquid Crystals*, 1st ed.; Springer: New York, NY, USA, 2001.
15. Goodby, J.W. Symmetry and Chirality in Liquid Crystals. In *Handbook of Liquid Crystals*, 1st ed.; Demus, D., Goodby, J.W., Gray, G.W., Spiess, H.-W., Vill, V., Eds.; Wiley-VCH: Weinheim, Germany, 1998; Volume 1, pp. 115–132.
16. Seki, A.; Funahashi, M. Photovoltaic Effects in Ferroelectric Liquid Crystals based on Phenylterthiophene Derivatives. *Chem. Lett.* **2016**, *45*, 616–618. [CrossRef]

17. Seki, A.; Funatsu, Y.; Funahashi, M. Anomalous photovoltaic effect based on molecular chirality: Influence of enantiomeric purity on the photocurrent response in π-conjugated ferroelectric liquid crystals. *Phys. Chem. Chem. Phys.* **2017**, *19*, 16446–16455. [CrossRef] [PubMed]
18. Seki, A.; Funahashi, M. Chiral photovoltaic effect in an ordered smectic phase of a phenylterthiophene derivative. *Org. Electron.* **2018**, *62*, 311–319. [CrossRef]
19. Seki, A.; Yoshio, M.; Mori, Y.; Funahashi, M. Ferroelectric Liquid-Crystalline Binary Mixtures Based on Achiral and Chiral Trifluoromethylphenylterthiophenes. *ACS Appl. Mater. Interfaces* **2020**, *12*, 53029–53038. [CrossRef]
20. Mulder, D.J.; Schenning, A.P.H.J.; Bastiaansen, C.W.M. Chiral-nematic liquid crystals as one dimensional photonic materials in optical sensors. *J. Mater. Chem. C* **2014**, *2*, 6695–6705. [CrossRef]
21. Hartmann, W.J.A.M. Ferroelectric Liquid Crystal Displays for Television Application. *Ferroelectrics* **1991**, *122*, 1–26. [CrossRef]
22. Funahashi, M. Chiral Liquid Crystalline Electronic Systems. *Symmetry* **2021**, *13*, 672. [CrossRef]
23. Shimizu, Y.; Oikawa, K.; Nakayama, K.; Guillon, D. Mesophase semiconductors in field effect transistors. *J. Mater. Chem.* **2007**, *17*, 4223–4229. [CrossRef]
24. Pisula, W.; Zorn, M.; Chang, J.Y.; Müllen, K.; Zentel, R. Liquid Crystalline Ordering and Charge Transport in Semiconducting Materials. *Macromol. Rapid Commun.* **2009**, *30*, 1179–1202. [CrossRef] [PubMed]
25. Funahashi, M. Development of Liquid-Crystalline Semiconductors with High Carrier Mobilities and Their Application to Thin-film Transistors. *Polym. J.* **2009**, *41*, 459–469. [CrossRef]
26. O'Neill, M.; Kelly, S.M. Ordered Materials for Organic Electronics and Photonics. *Adv. Mater.* **2011**, *23*, 566–584. [CrossRef] [PubMed]
27. Seki, A.; Funahashi, M. Nanostrucure Formation Based on the Functionalized Side Chains in Liquid-Crystalline Heteroaromatic Compounds. *Heterocycles* **2016**, *92*, 3–30.
28. Kato, T.; Yoshio, M.; Ichikawa, T.; Soberats, B.; Ohno, H.; Funahashi, M. Transport of ions and electrons in nanostructured liquid crystals. *Nat. Rev. Mater.* **2017**, *2*, 17001. [CrossRef]
29. Hori, T.; Miyake, Y.; Yamasaki, N.; Yoshida, H.; Fujii, A.; Shimizu, Y.; Ozaki, M. Solution Processable Organic Solar Cell Based on Bulk Heterojunction Utilizing Phthalocyanine Derivative. *Appl. Phys. Express* **2010**, *3*, 101602. [CrossRef]
30. Shin, W.; Yasuda, T.; Watanabe, G.; Yang, Y.S.; Adachi, C. Self-Organizing Mesomorphic Diketopyrrolopyrrole Derivatives for Efficient Solution-Processed Organic Solar Cells. *Chem. Mater.* **2013**, *25*, 2549–2556. [CrossRef]
31. Hassheider, T.; Benning, S.A.; Kitzerow, H.-S.; Achard, M.-F.; Bock, H. Color-Tuned Electroluminescence from Columnar Liquid Crystalline Alkyl Arenecarboxylates. *Angew. Chem. Int. Ed.* **2001**, *40*, 2060–2063. [CrossRef]
32. Aldred, M.P.; Contoret, A.E.A.; Farrar, S.R.; Kelly, S.M.; Mathieson, D.; O'Neill, M.; Tsoi, W.C.; Vlachos, P. A Full-Color Electroluminescent Device and Patterned Photoalignment Using Light-Emitting Liquid Crystals. *Adv. Mater.* **2005**, *17*, 1368–1372. [CrossRef]
33. Benning, S.A.; Oesterhaus, R.; Kitzerow, H.-S. Polarized electroluminescence of a discotic mesogenic compound. *Liq. Cryst.* **2004**, *31*, 201–205. [CrossRef]
34. van Breemen, A.J.J.M.; Herwig, P.T.; Chlon, C.H.T.; Sweelssen, J.; Schoo, H.F.M.; Setayesh, S.; Hardeman, W.M.; Martin, C.A.; de Leeuw, D.M.; Valeton, J.J.P.; et al. Large Area Liquid Crystal Monodomain Field-Effect Transistors. *J. Am. Chem. Soc.* **2006**, *128*, 2336–2345. [CrossRef] [PubMed]
35. Funahashi, M.; Zhang, F.; Tamaoki, N. High Ambipolar Mobility in a Highly Ordered Smectic Phase of a Dialkylphenylterthiophene Derivative That Can Be Applied to Solution-Processed Organic Field-Effect Transistors. *Adv. Mater.* **2007**, *19*, 353–358. [CrossRef]
36. Pisula, W.; Menon, A.; Stepputat, M.; Lieberwirth, I.; Kolb, U.; Tracz, A.; Sirringhaus, H.; Pakula, T.; Müllen, K. A Zone-Casting Technique for Device Fabrication of Field-Effect Transistors Based on Discotic Hexa-*peri*-hexabenzocoronene. *Adv. Mater.* **2005**, *17*, 684–689. [CrossRef]
37. Funatsu, Y.; Sonoda, A.; Funahashi, M. Ferroelectric liquid-crystalline semiconductors based on a phenylterthiophene skeleton: Effect of introduction of oligosiloxane moieties and photovoltaic effect. *J. Mater. Chem. C* **2015**, *3*, 1982–1993. [CrossRef]
38. Glass, A.M.; von der Linde, D.; Negran, T.J. High-voltage bulk photovoltaic effect and the photorefractive process in $LiNbO_3$. *Appl. Phys. Lett.* **1974**, *25*, 233–235. [CrossRef]
39. Fridkin, V.M.; Popov, B.N. The Anomalous Photovoltaic Effect and Photoconductivity in Ferroelectrics. *Phys. Status Solidi A* **1978**, *46*, 729–733. [CrossRef]
40. Yuan, Y.; Xiao, Z.; Yang, B.; Huang, J. Arising applications of ferroelectric materials in photovoltaic devices. *J. Mater. Chem. A* **2014**, *2*, 6027–6041. [CrossRef]
41. Butler, K.T.; Frost, J.M.; Walsh, A. Ferroelectric materials for solar energy conversion: Photoferroics revisited. *Energy Environ. Sci.* **2015**, *8*, 838–848. [CrossRef]
42. Sotome, M.; Nakamura, M.; Fujioka, J.; Ogino, M.; Kaneko, Y.; Morimoto, T.; Zhang, Y.; Kawasaki, M.; Nagaosa, N.; Tokura, Y.; et al. Spectral dynamics of shift current in ferroelectric semiconductor SbSI. *Proc. Natl. Acad. Sci. USA* **2019**, *116*, 1929–1933. [CrossRef]
43. Morimoto, T.; Nakamura, M.; Kawasaki, M.; Nagaosa, N. Current-Voltage Characteristic and Shot Noise of Shift Current Photovoltaics. *Phys. Rev. Lett.* **2018**, *121*, 267401. [CrossRef] [PubMed]

44. Nakamura, M.; Hatada, H.; Kaneko, Y.; Ogawa, N.; Tokura, Y.; Kawasaki, M. Impact of electrodes on the extraction of shift current from a ferroelectric semiconductor SbSI. *Appl. Phys. Lett.* **2018**, *113*, 232901. [CrossRef]
45. Sugita, A.; Suzuki, K.; Tasaka, S. Ferroelectric properties of a triphenylene derivative with polar functional groups in the crystalline state. *Phys. Rev. B* **2004**, *69*, 212201. [CrossRef]
46. Sasabe, H.; Nakayama, T.; Kumazawa, K.; Miyata, S.; Fukuda, E. Photovoltaic Effect in Poly(vinylidene fluoride). *Polym. J.* **1981**, *13*, 967–973. [CrossRef]
47. Zhang, C.; Nakano, K.; Nakamura, M.; Araoka, F.; Tajima, K.; Miyajima, D. Noncentrosymmetric Columnar Liquid Crystals with the Bulk Photovoltaic Effect for Organic Photodetectors. *J. Am. Chem. Soc.* **2020**, *142*, 3326–3330. [CrossRef]
48. Funahashi, M. High open-circuit voltage under the bulk photovoltaic effect for the chiral smectic crystal phase of a double chiral ferroelectric liquid crystal doped with a fullerene derivative. *Mater. Chem. Front.* **2021**, *5*, 8265–8274. [CrossRef]
49. Wurzbach, I.; Rothe, C.; Bruchlos, K.; Ludwigs, S.; Giesselmann, F. Shear alignment and 2D charge transport of tilted smectic liquid crystalline phases—XRD and FET studies. *J. Mater. Chem. C* **2019**, *7*, 2615–2624. [CrossRef]
50. Yelamaggad, C.V.; Shashikala, I.S.; Hiremath, U.S.; Shankar Rao, D.S.; Prasad, S.K. Liquid crystal dimers possessing chiral rod-like anisometric segments: Synthesis, characterization and electro-optic behaviour. *Liq. Cryst.* **2007**, *34*, 153–167. [CrossRef]
51. Sund, P.; Pettersson, F.; Österbacka, R.; Wilén, C.-E. Conductivity, interaction and solubility of hetero-bifunctional end-capped β,β′-dihexylsubstituted sexithiophenes. *J. Appl. Polym. Sci.* **2018**, *135*, 46830. [CrossRef]
52. Swamy, K.C.K.; Kumar, N.N.B.; Balaraman, E.; Kumar, K.V.P.P. Mitsunobu and Related Reactions: Advances and Applications. *Chem. Rev.* **2009**, *109*, 2551–2651. [PubMed]
53. Shi, Y.-J.; Hughes, D.L.; McNamara, J.M. Stereospecific synthesis of chiral tertiary alkyl-aryl ethers via Mitsunobu reaction with complete inversion of configuration. *Tetrahedron Lett.* **2003**, *44*, 3609–3611. [CrossRef]
54. Bouchta, A.; Nguyen, H.T.; Achard, M.F.; Hardouin, F.; Destrade, C.; Twieg, R.J.; Maaroufi, A.; Isaert, N. New TGB_A series exhibiting a S_C*$S_A$$S_A$*N* phase sequence. *Liq. Cryst.* **1992**, *12*, 575–591. [CrossRef]
55. Hall, A.W.; Lacey, D.; Hill, J.S.; Blackwood, K.M.; Jones, M.; McDonnell, D.G.; Sage, I.C. Synthesis and evaluation of a series of novel 2-substituted poly(allylalcohol) side chain liquid crystalline oligomers exhibiting ferroelectricity. *Liq. Cryst.* **1996**, *20*, 437–447. [CrossRef]
56. McCubbin, A.J.; Snieckus, V.; Lemieux, R.P. Ferroelectric liquid crystals with fluoro- and aza-fluorenone cores: The effect of stereo-polar coupling. *Liq. Cryst.* **2005**, *32*, 1195–1203. [CrossRef]
57. Sackmann, H.; Demus, D. The Problems of Polymorphism in Liquid Crystals. *Mol. Cryst. Liq. Cryst.* **1973**, *21*, 239–273. [CrossRef]
58. Funahashi, M.; Hanna, J. High ambipolar carrier mobility in self-organizing terthiophene derivative. *Appl. Phys. Lett.* **2000**, *76*, 2574–2576. [CrossRef]
59. Rao, P.B.; Rao, N.V.S.; Pisipati, V.G.K.M. The Smectic F Phase in nO.m Compounds. *Mol. Cryst. Liq. Cryst.* **1991**, *206*, 9–15. [CrossRef]
60. Ouchi, Y.; Uemura, T.; Takezoe, H.; Fukuda, A. Molecular Reorientaion Process in Chiral Smectic I Liquid Crystal. *Jpn. J. Appl. Phys.* **1985**, *24*, 893–895. [CrossRef]
61. Uemoto, T.; Yoshino, K.; Inuishi, Y. Electrical and Optical Properties of Ferroelectric Liquid Crystals and Influence of Applied Pressure. *Mol. Cryst. Liq. Cryst.* **1981**, *67*, 137–152. [CrossRef]
62. Doi, T.; Sakurai, Y.; Tamatani, A.; Takenaka, S.; Kusabayashi, S.; Nishihata, Y.; Terauchi, H. Thermal and X-Ray Diffraction Studies of Liquid Crystals incorporating a Perfluoroalkyl Group. *J. Mater. Chem.* **1991**, *1*, 169–173. [CrossRef]
63. Lee, M.; Cho, B.-K.; Kim, H.; Yoon, J.-Y.; Zin, W.-C. Self-Organization of Rod–Coil Molecules with Layered Crystalline States into Thermotropic Liquid Crystalline Assemblies. *J. Am. Chem. Soc.* **1998**, *120*, 9168–9179. [CrossRef]
64. Ting, C.-H.; Hsu, C.-S. Synthesis and photoluminescence property of polyacetylenes containing liquid crystalline side groups. *J. Polym. Res.* **2001**, *8*, 159–167. [CrossRef]
65. Ting, C.-H.; Chen, J.-T.; Hsu, C.-S. Synthesis and Thermal and Photoluminescence Properties of Liquid Crystalline Polyacetylenes Containing 4-Alkanyloxyphenyl trans-4-Alkylcyclohexanoate Side Groups. *Macromolecules* **2002**, *35*, 1180–1189. [CrossRef]
66. Vergara-Toloza, R.O.; Soto-Bustamante, E.A.; Gonzalez-Henriquez, C.M.; Haase, W. Side chain liquid crystalline composites, occurrence of interdigitated bilayer smectic C phases. *Liq. Cryst.* **2011**, *38*, 911–916. [CrossRef]
67. Zhu, P.; Wu, L.; Liu, W.; Li, B.; Li, Y.; Yang, Y. Methylation driven molecular packing difference at the smectic phases of a series of pyridinium-based chiral ionic liquid crystals. *Mol. Cryst. Liq. Cryst.* **2021**, *731*, 55–65. [CrossRef]
68. Hsu, H.-F.; Chien, S.-J.; Chen, H.-H.; Chen, C.-H.; Huang, L.-Y.; Kuo, C.-H.; Chen, K.-J.; Ong, C.W.; Wong, K.-T. Mesogenic and optical properties of α,α′-bis(4-alkoxyphenylethynyl)oligothiophenes. *Liq. Cryst.* **2005**, *32*, 683–689. [CrossRef]